SCIENTIFIC REPORTS

OPEN

SUBJECT AREAS:
SEISMOLOGY
CIVIL ENGINEERING
APPLIED PHYSICS
CHARACTERIZATION AND ANALYTICAL TECHNIQUES

Received
19 February 2013

Accepted
16 April 2013

Published
8 May 2013

Correspondence and requests for materials should be addressed to H.O.G. (h.o.ghaffari@gmail.com)

Acoustic-Friction Networks and the Evolution of Precursor Rupture Fronts in Laboratory Earthquakes

H. O. Ghaffari & R. P. Young

Department of Civil Engineering and Lassonde Institute, University of Toronto, 170 College Street, Toronto, ON M5S3E3Canada.

The evolution of shear rupture fronts in laboratory earthquakes is analysed with the corresponding functional networks, constructed over acoustic emission friction-patterns. We show that the mesoscopic characteristics of functional networks carry the characteristic time for each phase of the rupture evolution. The classified rupture fronts in network states–obtained from a saw-cut fault and natural faulted Westerly granite - show a clear separation into three main groups, indicating different states of rupture fronts. With respect to the scaling of local ruptures' durations with the networks' parameters, we show that the gap in the classified fronts could be related to the possibility of a separation between slow and regular fronts.

Recently, a series of laboratory earthquake/friction experiments have reported observing complex slip-front evolution in terms of the speed and the general configurations of the ruptures[1–12]. Although some aspects of the laboratory (or field observations) had been predicted through numerical experiments[9–21], the new evidence necessitates a more precise analysis of the results and observations. In considering the complexity of rupture fronts, the super-shear fronts, slow fronts and mixture ruptures (i.e., transitions in rupture modes) as well as precursor events preceding the main stick-slip events have been of interest. Study of precursor events in laboratory earthquakes -as the arrested or potential of transition rupture- revealed a new type of slow dynamic of the frictional interfaces. Ohnaka and Fineberg[1,11] reported a slow front evolution during frictional slipping, which was followed by several other numerical and experimental works[3,5,9,11,13,17,18,28]. In particular, it was proposed that the occurrence of slow ruptures on a laboratory scale accompanies weak acoustic amplitude signatures in radiated acoustics[1,2]. A recent robust modeling highlighted the intrinsic nature of slow ruptures that resulted from rate-and-state friction laws, which led to the prediction of a new velocity scale as the minimum rate of slow rupture propagation[17,18]. The observed slow ruptures can be compared with slow earthquakes as a new topic while their mechanisms are not completely understood[18,22–28]. Also, analyzing the collection of large-scale earthquakes regarding source duration and the final displacement of events has shown a clear gap between regular earthquakes and silent earthquakes, representing different classes of slip front propagation[22,27].

From another perspective, the study of the evolution of frictional interfaces with respect to the passage of Sub-Rayleigh precursor rupture fronts on poly methyl methacrylate (PMMA) blocks showed several phases of the evolution from the arrested rupture fronts[6]. Fast approaching rupture tip leading to failure of asperity and large deformation proceeds with the fast slip while a time characteristic controls the distinguished phases. In this research, we show that functional acoustic networks also show the similar evolutionary phases while we investigate the rupture fronts from Westerly Granite. We speculate that the dynamic configurations of multi-channel acoustic emission waveforms in appropriate network-parameter spaces show different possible classes of rupture regimes, encoded in the corresponding constructed functional networks from the recorded signals. Also, we provide solid observations of the gap between regular and slow fronts while the rupture fronts are analyzed in terms of their local-source duration and network-local energy flow index. Our results clearly indicate that precursor events from dry frictional interface follow a universal trend in corresponding network states, separating their features from random (null) networks.

Results

Our data set includes the recorded discrete and continuous waveforms (i.e., acoustic emissions-AEs) using 16 piezoelectric transducers from a saw-cut sample of Westerly granite (LabEQ1), under triaxial loading (Fig. 1)[31,32]. The saw cut was at a 60 degree angle and polished with silicon carbide 220 grit. Each triggered event had the

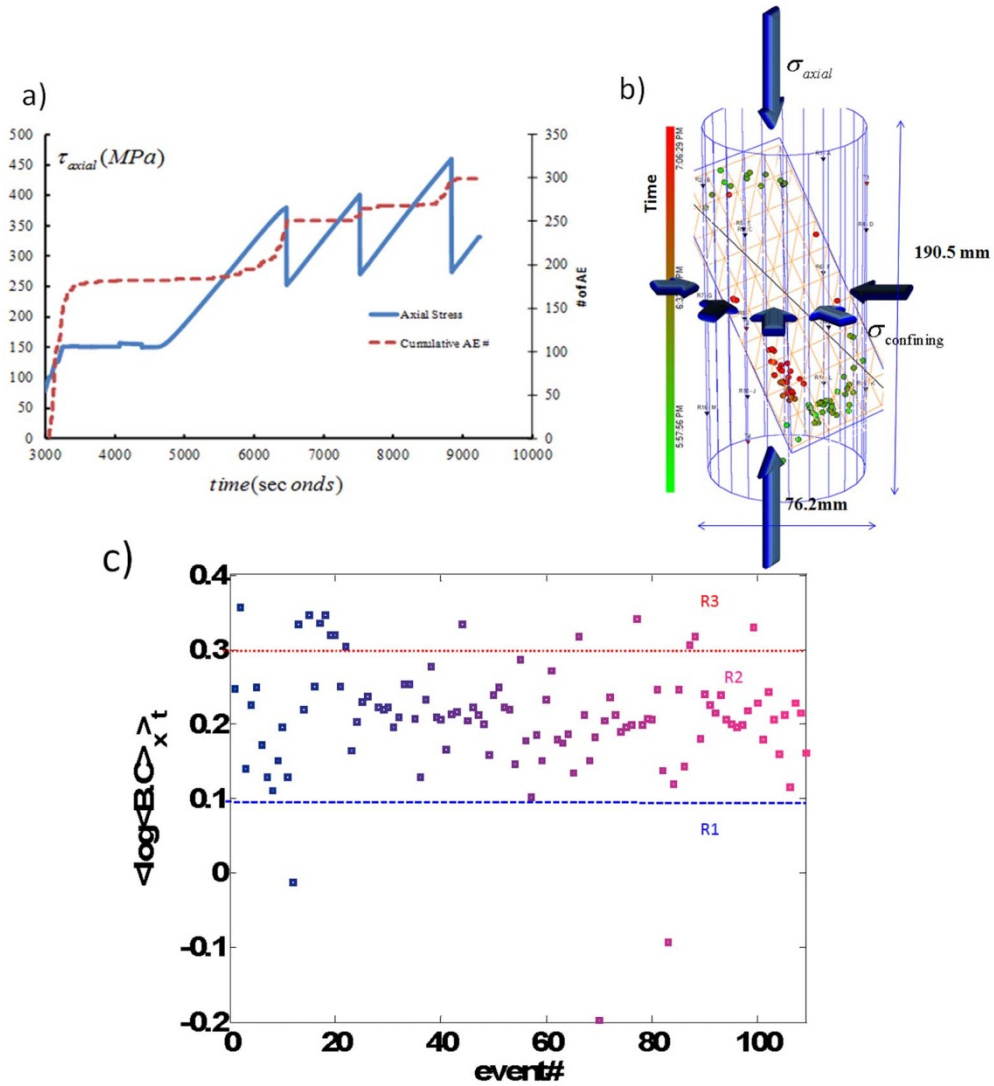

Figure 1 | The study of arrested rupture fronts with functional acoustic-friction networks reveals the evolution of acoustic events. (a), Three cycles of main stick-slip events in LabEQ1 and cumulative acoustic events[31]. (b), The geometry of the smooth fault embedded in a cylindrical westerly Granite and the source locations of the recorded events with the occurrence time of each event as the color bar. The triangles show the position of piezoelectric transducers. (c), Mapping the recorded events in $\overline{\log <B.C>}$ versus the event's number shows some abnormal fronts (R1 and R3). Ruptures with relatively high energy allocate lower $\overline{\log <B.C>}$.

duration of 204.8 μs (recorded at 5 MHz), while the three main stick-slip events occurred with shear stress drops of 54, 56 and 79 MPa. The experiment was servo-controlled using an axial strain rate of $5\times10^{-6}\ s^{-1}$. The confining stress was maintained at 150 MPa for three reported main stick-slip events, producing 109 located- rupture fronts events. The second data set (LabEQ2) includes the results of the two main cycles of loading –unloading (stick-slip) of Westerly granite on a preexisting natural fault by loading at constant confining pressure. A natural rough fault was created using a triaxial loading system at constant confining pressure of 50 MPa and with acoustic emission feedback control. The two main phases of stick-slip were accomplished in 200 MPa and 150 MPa confinement pressure, respectively. The driving strain rate was identical to the LabEQ1. We reported an analysis of over 8000 recorded rupture fronts from two main stick-slip events. Using the aforementioned data set, we constructed the corresponding functional networks (see the methods part) and studied their properties such as betweenness centrality (B.C), maximum modularity (Q), with-in module degree (z-score), maximum eigenvalue of Laplacian of connectivity matrix ($\lambda_{\max.}$) and inverse participation ratio (P). The evolutions of corresponding functional friction networks are rationalized in terms of their local and mean attributes (i.e., spatial and temporal mean).

Starting with LabEq.1data set, we show that most of the recorded events exhibit a universal trend of the evolution in terms of their modularity trend (Fig. 2a, b). Considering the modularity as the mean response of the whole nodes (corresponding to stations) and the rough collapse of the data (Fig. 2b), one can recognize the 4 main evolutionary phases during 204 μs time-window (where the calculated maximum modularity value varies between 0.001 and 0.49). Phase I is quantified with the fast drop of the modularity and the approaching to the minimum modularity. We assign this phase to the approaching and large deformation of the asperities (or asperity). In other words, the mean dramatic deformation of a "node" is encoded in fast drop of the modularity while mean local energy flow index ($<B.C>_x$-Eq.2 Methods part) is also reaching to minimum value. Our investigation on ~50 regular events showed this phase has duration between $\sim 8\pm 4\ \mu s$ (we will show this interval is longer in slow deformation). The magnitude of this drop is scaled with the maximum recorded of voltage from the employed piezoelectric

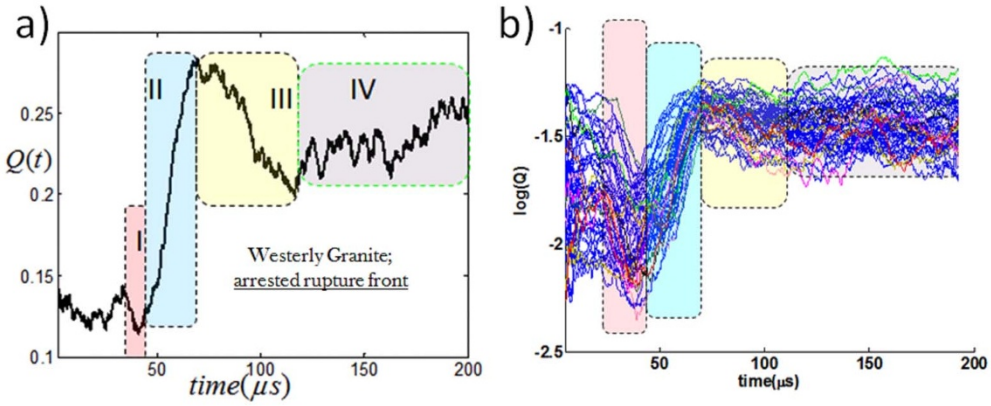

Figure 2 | General dynamic of modularity index of precursor events. (a), A typical evolution of the modularity index of a precursor rupture front from LabEQ1. 4 main phases are: approaching and failure time (Phase I, $Q(t) \rightarrow Q_{\min}(t)$), rapid growth of modularity (Phase II), slow drop of modularity (phase III) and slow decay (Phase IV). (b), An approximate collapse of the modularity values for recorded regular ruptures (i.e., ~20 events from R2 in figures 2 and 3). The duration of phase I and II are nearly constant in approximating 5–10 μs and 20–30 μs respectively (also see Fig. S4–S6).

sensors. Larger deformation and crushing asperities with significant damages are encoded in big amount of the drop in the modularity value. A rapid modularity growth phase is shown in the characteristics of the phase 2 with the duration of $\sim 25 \pm 7$ μs. A possible explanation of the fast rising time is the occurrence of the rapid slip of broken asperities while after a nearly constant timescale a gradual drop is observed (Phase III). The next following phase (IV) is generally decaying much more slowly than previous phase, with a small range of fluctuations in Q. The duration of this phase is the longest in comparison with the previous phases. The decay rate of this phase is significantly higher for Lab.EQ.2, indicating the role of the heterogeneity of rough-faults in suppressing slip signals (Fig. S4, S5, S6). Regardless of the real physical meaning of Q, the similarity of the evolutionary phases of the network-parameter space of the precursor events to the reported slip profiles from glassy materials (such as PMMA)[6], shows that the fracture inducing weakening is a general scenario in frictional interfaces. With using modular profiles, we also proved the well-known fact on asymmetric pulse shape of crackling noise[39]. We found that the rate of evolution of phase II always is higher than the last evolutionary phase, indicting asymmetric universal shape of the shown profiles. The origin of this asymmetric shape is related to threshold strengthening[40] or cooling down phase, encoded in phase III (see supplementary document). Indeed, our results completely match with the reported asymmetric moment rate pulse shape from natural earthquakes[40]. We also compared the networks obtained from experimental data with ensembles of null-model networks (see supplementary document). These results illustrate that the friction networks have different network attributes than the random networks.

Considering the spatio-temporal mean value of betweenness centrality over Lab.EQ.1, we find the three distinguished classes of rupture fronts (Fig. 1c). The main stick-slip events are mapped into an R1 zone which indicates the high amplitude activities of acoustic emission waveforms. This zone generally accompanies the visible records of displacements, mostly recorded in stick-slip periods. The most recorded events are encoded in R2, where we classify them as "regular" events. A few of the precursor rupture fronts allocate R3 class. We found that unusually long localizations of eigenvectors ($\langle P \rangle_x$-Eq.2 in Methods part) regarding regular duration (such as R2 ruptures) with high maximum eigenvalues are the highlighted features of R3 (Fig. 3.a and d-also see Fig. S5). The long term of localization is nearly 2 to 5 times the regular localization period (i.e., R2 ruptures (Fig. 3.c)). This picture is compatible with the longer duration of phase I (Fig. S5d). We carefully tested the amplitudes of acoustic waveforms from the R3 events which indicated a weak-long activity of the signals in most of the stations. We observe these features at all locations traversed by all well-located triggered rupture fronts as have been shown in Fig. 1.b. Another feature which distinguishes R3 events from R2 fronts is shown in Fig. 3a: a unique gap between R2 and R3 in $\overline{\log < B.C >} - \bar{\lambda}_{\max}$ parameter space. All evidence implies that the R3 fronts are slow ruptures with distinguished separation from regular ruptures, as it has been indicated in natural large slow earthquakes[22,27].

Matching the far-field driving stress field with the corresponding individual arrested rupture fronts(triggered at the same time), reveals a nearly power-law decay of the temporal mean of the modularity versus shear stress per each cycle of loading in Lab.EQ.1(Fig. 3.b): $\tau_s \simeq -0.33 \times 10^3 \log \bar{Q}$ in which $\bar{Q}$ is the temporal mean over all phases. In other words, approaching the main stick-slip event is accompanied with a lower mean temporal modularity index, indicting possible longer phase I (or significant amount of the drop from the rest state) or decreasing the peak value of the maximum modularity in phase I (also see Fig. S7). This shows how micro-ruptures, resulted in the recorded acoustic emission waveforms evolve regarding the uniform shear stress. Assuming the validation of the Amontons-Coulomb law ($\tau_S = \mu_S \sigma_N$) in the scale of the arrested fronts, we reach to: $\mu_S \sim \bar{Q}^{-\xi}$ for a constant normal loading, indicating that local static friction is possibly correlated with the details of the rupturing and slipping of the local fronts, comparable with the recent experimental results[9].

For all collapsed events in $\overline{\log < B.C >} - \bar{\lambda}_{\max}$, we can assign a simple power law as well as: $\overline{\lambda_{\max}} \propto \overline{\log < B.C >}^{-\beta}$ which also holds for Lab.EQ.2 data set (Fig. 4a). In contrast to Lab.EQ.1, events from the natural-rough fault does not show the separation and clear gap of R3 from R2 while transition to R2 is observed in terms of the decrease in the critical exponent of the scaling relation (Fig. 4a-inset). This transition also can be followed in terms of the density of the events in R3 versus R2 (Fig. 4b). While for Lab.Eq1, most of R3 fronts occur in initial loading steps, the temporal distribution of R3 in Lab.EQ.2 is not limited to a specific time step. To connect the detected evolutionary phases to the classified events, we plotted the rate of the last phase (IV) versus the maximum modularity per each event, showing the same classification of events (Fig. S5). This demonstration strongly proves that the relatively weak events have smaller rate of decay and longer phase I, indicating a slow deformation and longer source duration, supporting the results of Fig. 3. This property is the key to the separation of slow events from other events. The cross-over from slow deformation to regular events also is accompanied

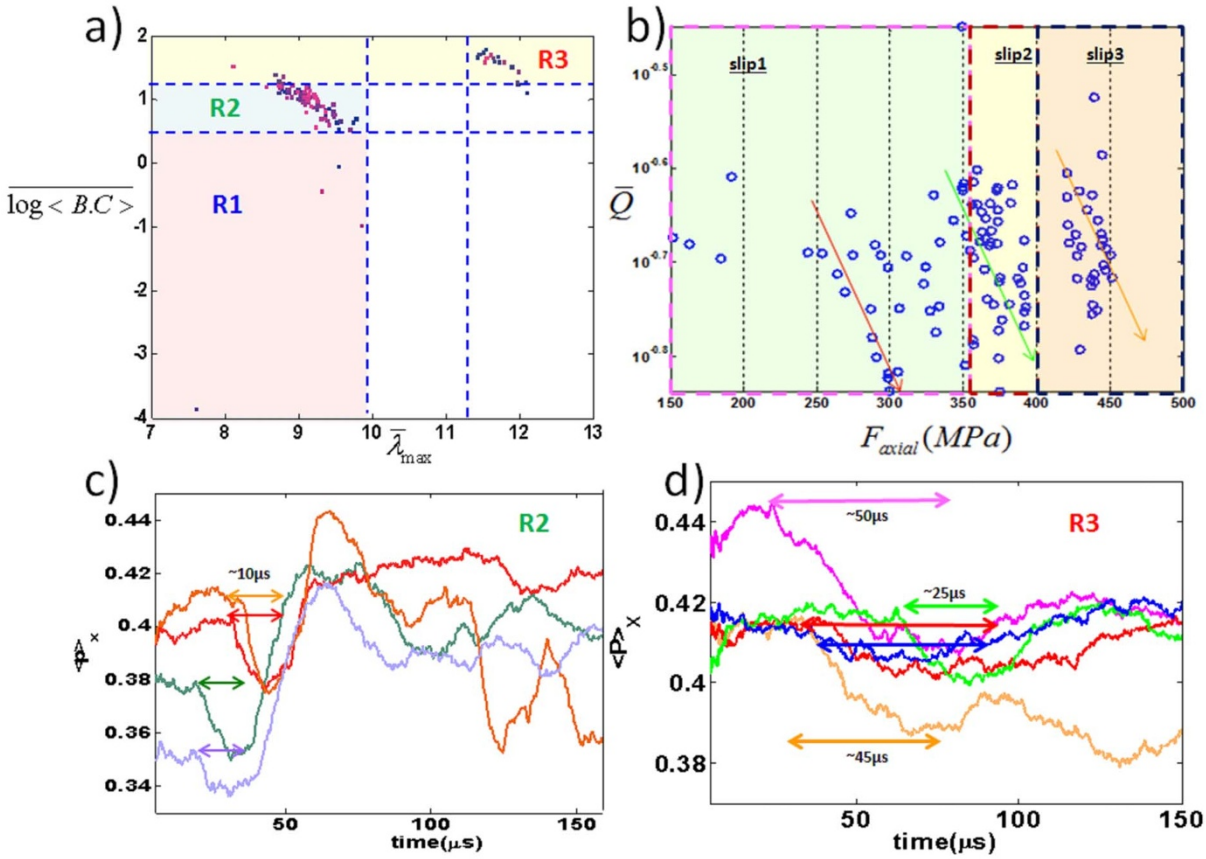

Figure 3 | Classified detachment fronts in network parameter space. (a), Mapping 109 events during 204 μs time-window from LabEQ1 on the spatio-temporal mean of betweenness centrality -mean of maximum eigenvalues of Laplacain parameter space. (b), The evolution of $\bar{Q}$ versus axial stress (MPa) as the remote driving stress in the smooth-fault experiment through 3 cycles of main stick-slip as has been shown in Figure 2a. A simple logarithmic relation per each cycle can be assigned as: $F_{axial} \simeq -0.33 \times 10^3 \log \bar{Q}$ indicating that generally the lower values of $\bar{Q}$ occur in relatively higher driving shear stress. (c), A typical characteristic of the regular recorded waveforms with respect to the average inverse participation coefficient shows ~10 μs sharp drop of localization of eigenvectors (corresponding to the phase I in figure 1a). (d), Recorded fronts in R3 cluster show longer phase I (~25–50 μs). $(\overline{\ldots})$ and $<\ldots>_x$ indicate the average over 204 μs per each recorded rupture front and the mean over nodes, respectively (Also see Fig. S5)

with the dramatic change of the power-law exponents in other network-parameter spaces (Fig. S5c), showing a possible first order transition of ruptures from slow to regular ones as well as transition to critical rupture regimes for tensile[41] or shear ruptures[8,12].

Investigation into the recurrence times of precursor ruptures in each class shows that the observation of the density changes indeed is mapped into the waiting times (Fig. S10). Considering Lab.EQ.2, most of the events in R2 zone show waiting times <200 ms while events in R3 point out a combination of <200 ms to 2000 ms. In ruptures with the signature of significant release of energy (R1 class in comparison with other classes), the mean of the waiting times are around ~2000 ms. The main implication of three main classes of recurrence times probably could be a point of more investigation on the role of precursor events on healing or aging phenomena on frictional interfaces. Events with a longer waiting time allocate a certain class of the introduced parameter spaces (i.e., R1), while a shorter recurrence time indicates rupture fronts with weaker amplitude, possibly small stress drop per each front.

Discussion

The applications of complex networks on multi-stationary accused laboratory earthquakes regarding precursor rupture fronts were addressed in this research. For the first time, we presented a universal picture of acoustic waveforms resulted from friction phenomena. We recognized the main evolutionary phases of each rupture front, imprinting approaching rupture front, crashing or failure of asperity (nodes in networks) and slipping phases. This finding provides a general universal mechanism for the fracture weakening mechanism for precursor rupture fronts, implying an asymmetric shape of the pulses as it has been confirmed in natural earthquakes for the average shape of the moment rate pulses. The recorded signals from rough-frictional interface show a faster decay of slip-phase rather than smooth-faults while generally ruptures with higher maximum modularity decay faster. The scaling of temporal mean modularity with the shear stress was observed in the smooth fault, indicating the dependency of local static friction to fronts' phases, confirming recent experimental results on PMMA. Furthermore, the classification of the recorded rupture fronts using the mesoscopic (*i.e.,* modular features) and transport characteristics of friction networks as well as their relations to the evolutionary phases of pulses-revealed three main rupture fronts. The analyzed events from smooth and rough faults portrayed a universal trend of the ruptures' evolution where the recorded weak acoustic waveforms were encoded in high modularity index within the separated distinct clusters with long-duration in rupturing phase (i.e., local source duration). The separated cluster with scatter events and the signature of long tail of pulses-was related to the observation of slow ruptures in natural earthquakes, confirming a slow deformation phase. Obviously, with respect to the clipping amplified acoustic waveforms for events with relatively high release of energy (see figure S9), we cannot investigate slow events in large numbers of seismic moments. Interestingly, the analysis of over 8000 rupture fronts showed that the functional friction networks are

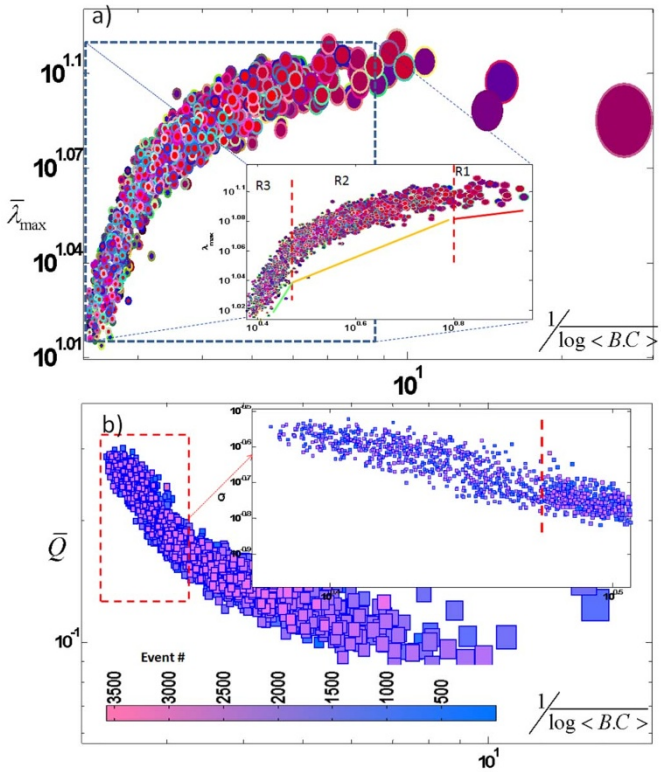

Figure 4 | Precursor events from the evolution of rough frictional interface. Evolution of rupture fronts in a rough fault (LabEQ2) through the first cycle of loading in (a), $\frac{1}{\overline{\log < B.C >}} - \overline{< \lambda_{max} >}$ parameter space for ~3500 recorded acoustic emission events; a critical exponent such as β in $\overline{< \lambda_{max} >} \sim \overline{\log < B.C >}^{-\beta}$ can be defined as it has been shown in the inset. The size of the circles corresponds to the maximum root mean square of the amplitudes of all piezoelectric sensors. (b), $\frac{1}{\overline{\log < B.C >}} - \overline{Q}$ for the same events. Inset shows a transition to R_2 (*i.e.*, regular events) occurs after a threshold level (also see Fig. S6 for loading configurations and Fig. S7 for the second cycle of the loading). Also see Fig. S5 and Fig. S.9.

not random networks (in comparison with appropriate null models) and imprint a unique signature in different network parameter spaces. This proves that the recorded pulses are generally separated from the system noise, helping to develop a possible stochastic network models on precursor events. The recurrence time of each class in the introduced scalar parameter space was related to the maximum modularity of the events in that class: generally high energy precursor events have longer waiting times while very weak rupture fronts may have abnormally short or long waiting time. The application of the presented methods on natural earthquakes and the comparison of their features with the laboratory weak-rupture fronts as well as employing other mapping techniques of time series to network spaces –including weighted and directed networks-and comparing the results with the presented algorithm in this study, will be our next project.

Methods

We proposed the following methods to characterize the interface evolutions within the available data set. To set up a non-directed network (as the class of recurrence networks[49]), we used a simplified version of the meta-time series method[33] in which the multi-channel (station), simultaneously-recorded time series was mapped onto a proper network. The method was used over the recorded time-series from acoustic transducers. A similar method has been used on real-time contact areas and apertures of frictional interfaces[29,30]. Other techniques-also-have been introduced into the study of time series analysis, such as the approaches based on the concept of a quasi-periodic cycle[43] correlations[44] visibility[45] transition probabilities[46] recurrence analysis (phase-space reconstruction)[47–49]. The main difference of the employed algorithm in this study is using all time series at the same time (i.e., sensors) instead of just analysis of one time-series. From this perspective, the constructed networks (see the below) are in analogy with functional brain networks[50]. Indeed, the introduced methods in the aforementioned references can be used to construct the networks in each time step, however we have used the simplest metric to construct friction networks.

We started with the normalization of waveforms in each station and then the division of *N*- recorded time series with the length of *T* into *m* segments. The *j*th segment from *i*th time series ($1 \le i \le N$) denoted by $x^{i,j}(t)$ was compared with $x^{k,j}(t)$ to make an edge among the aforementioned segments. If the *j*th segment of the *i*th and *k*th time series are "close" enough to each other, we set $a_{ik}(j) = 1$ otherwise $a_{ik}(j) = 0$ in which $a_{ik}(j)$ is the component of the connectivity matrix. We use a "closeness" metric: $d(x^{i,j}(t), x^{k,j}(t)) = \sum_t \left\| x^{i,j}(t) - x^{k,j}(t) \right\|$. To choose a threshold level, we follow the employed method in[29,30], in which the minimum variation of local flow energy with the threshold level is considered as a criterion to the best threshold level. To precisely analyze a time series with the aforementioned methods and reduce possible errors due to the limited number of stations, we set $m = 1$ (equal to each recorded point). We also increased the size of the adjacency matrix with simple interpolation of *d* using cubic spline interpolation. The increasing of number of nodes generally did not change the presented results and just increased the quality of visualization of the results. Then for the acoustic-friction networks, the numbers of nodes were 50 and we kept the number of nodes as the constant value.

To proceed, we used several characteristics of networks. Each node was characterized by its degree k_i and the clustering coefficient. The clustering coefficient (as a fraction of triangles) is C_i defined as $C_i = \frac{2T_i}{k_i(k_i-1)}$ where T_i is the number of links among the neighbors of node *i* and k_i is the number of links. For a given network with *N* nodes, the degree of the node and Laplacian of the connectivity matrix are defined by $k_i = \sum_{j=1}^{N} a_{ij}$; $L_{ij} = a_{ij} - k_i \delta_{ij}$ where k_i, a_{ij}, L_{ij} are the degree of *i* th node, elements of a symmetric adjacency matrix, and the network Laplacian matrix, respectively. The eigenvalues Λ_α are given by $\sum_{j=1}^{N} L_{ij}\phi_j^{(\alpha)} = \Lambda_\alpha \phi_i^{(\alpha)}$, in which $\phi_i^{(\alpha)}$ is the *i* th eigenvector of the Laplacian matrix ($\alpha = 1,\ldots,N$). With this definition, all eigenvalues are non-positive values[42]. With sorting the indices $\{\alpha\}$ in decreasing order of the eigenvalues, we have: $0 = \Lambda_1 \ge \Lambda_2 \ge \ldots \ge \Lambda_N$ and we define $\lambda_{max} = (-\Lambda_N)$ as the maximum eigenvalue of the Laplacian of the network.

A scalar measure of the localization degree of a vector is called the inverse participation index. The inverse participation ratio as a criterion of the localization of eigenvectors is defined by[34]:

$$P(\phi^\alpha) = \frac{\sum_i (\phi_i^\alpha)^4}{(\sum_i (\phi_i^\alpha)^2)^2}; \quad \alpha = 1,\ldots,N \tag{1}$$

The maximum value of ***P*** shows that the vector has only one non-zero component. A higher value of ***P*** corresponds with a more localized vector. We also addressed the role of betweenness centrality (B.C) of a node as the measure of "load"[35]:

$$B.C_i = \frac{1}{(N-1)(N-2)} \sum_{\substack{h,j \\ h \ne j, h \ne i, j \ne i}}^{N} \frac{\rho_{hj}^{(i)}}{\rho_{hj}} \tag{2}$$

in which ρ_{hj} is the number of the shortest path between *h* and *j*, and $\rho_{hj}^{(i)}$ is the number of the shortest path between *h* and *j* that passes *i*. Because the shortest paths include edges as the pairs of highly spatiality-close variation of acoustic activities, B.C can be interpreted as a measure of local energy-information flow. We also use the networks' modularity characteristics. In particular, based on the role of a node in the network modules, each node is assigned to its within-module degree (or *z*-score, z_i) and its participation coefficient (P_i). High values of *Z* indicate how well-connected a node is to other nodes in the same module, and P is a measure of well-distribution of the node's links among different modules[36]. The modularity *Q*(i.e., objective function) is defined as[36–38]:

$$Q = \sum_{s=1}^{N_M} [\frac{l_s}{L} - \left(\frac{d_s}{2L}\right)^2], \tag{3}$$

in which N_M is the number of modules (clusters), $L = \frac{1}{2}\sum_i^N k_i$, l_s is the number of links in module and $d_s = \sum_i k_i^s$ (the sum of nodes degrees in module s). Using an optimization algorithm (we use Louvain algorithm[38]), the cluster with maximum modularity (*Q*) is detected. $Q \to 0$ if nodes are configured in a random way or all nodes are in a single module.

Following[36], If κ_i is the number of links of node *i* to other nodes in its module s_i and $z_i = \kappa_i - <\kappa_i>$ is the average of links on the nodes in the module, within-module degree (*Z*) is defined as: $z_i \propto \kappa_i - <\kappa_i>$. The division of z_i to the standard deviation of links in the assumed module represent the z-score. The participation coefficient (P) is defined as[36]: $P_i = 1 - \sum_{s=1}^{N_m} (\frac{\kappa_{is}}{k_i})^2$ in which κ_{is} is the number of edges of node *i* to nodes in module *s*.

The correlation of a node with the degree of neighbouring nodes is defined as assortatitive mixing index[35]:

$$r_k = \frac{<j_l k_l> - <k_l>^2}{<k_l^2> - <k_l>^2} \quad (4)$$

where it shows the Pearson correlation coefficient between degrees (j_l,k_l) and $<\bullet>$ denotes the average over the number of links in the network. High assortativity indicates the attraction of rich nodes to each other (i.e., hubs) and negative value of r presents disassortative attribute of nodes where "poor" nodes are attracted to hubs.

1. Rubinstein, S., Cohen, G. & Fineberg, J. Detachment fronts and the onset of dynamic friction. *Nature.* **430**, 1005–1009 (2004).
2. Rubinstein, S., Cohen, G. & Fineberg, J. Cracklike processes within frictional motion: Is slow frictional sliding really a slow process? *MRS Bulletin.* **33**, 1181–89 (2008).
3. Nielsen, S., Taddeucci, J. & Vinciguerra, S. Experimental observation of stick-slip instability fronts. *Geophys. J. Int.* **180**, 697 (2010).
4. Schubnel, A., Nielsen, S., Taddeucci, J., Vinciguerra, S. & Rao, S. Photo-acoustic study of subshear and supershear ruptures in the laboratory. *Earth Planet. Sci. Lett.*, **308**, 424–432 (2011).
5. Latour, S. *et al.* M. Ultrafast ultrasonic imaging of dynamic sliding friction in soft solids: The slow slip and the super-shear regimes. *EPL.* **96**, 59003 (2011).
6. Ben-David, O., Rubinstein, S. & Fineberg, J. Slip-Stick: The evolution of frictional strength. *Nature.* **463**, 76 (2010).
7. Ben-David, O., Cohen, G. & Fineberg, J. The dynamics of the onset of frictional slip. *Science.* **330**, 211 (2010).
8. Xia, K., Rosakis, A. J. & Kanamori, H. Laboratory earthquakes: the sub-Raleigh-to super-shear rupture transition. *Science* **303**, 1859–1861 (2004).
9. Ben-David, O. & Fineberg, J. Static friction coefficient is not a material constant. *Phys. Rev. Lett.* **106**, 254301 (2011).
10. Dieterich, J. H. & Kilgore, B. D. Direct observation of frictional contacts — new insights for state dependent properties. *Pure Appl. Geophys.* **143**, 283–302 (1994).
11. Ohnaka, M. & Shen, L. F. Scaling of the shear rupture process from nucleation to dynamic propagation: Implications of geometric irregularity of the rupturing surfaces. *J. Geophys. Res. B* **104**, 817–844 (1999).
12. Andrews, D. J. Rupture velocity of plane strain shear cracks. *J. Geophys. Res. B* **81**, 5679–5687 (1976).
13. Braun, O. M., Barel, I. & Urbakh, M. Dynamics of transition from static to kinetic friction. *Phys. Rev. Lett.* **103** (2009).
14. Rice, J. R., Lapusta, N. & Ranjith, K. Rate and state dependent friction and the stability of sliding between elastically deformable solids. *J. Mech. Phys. Solids* **49**, 1865–1898 (2001).
15. Dunham, E. M. Conditions governing the occurrence of supershear ruptures under slip-weakening friction. *J. geophys. Res.* **112**, B07302 (2007).
16. Das, S. & Aki, K. Numerical study of 2-dimensional spontaneous rupture propagation. *Geophys. J. R. Astron. Soc.* **50**, 643 (1977).
17. Bouchbinder, E., Brener, E. A., Barel, I. & Urbakh, M. Dynamics at the onset of frictional sliding. *Phys. Rev. Lett.* **107**, 235501 (2011).
18. Sinai, Y. B. E., Brener, A. & Bouchbinder, E. Slow rupture of frictional interfaces. *Geophys. Res. Lett.* **39**, L03308 (2012).
19. Burridge, R. & Knopoff, L. Model and theoretical seismicity. *Bulletin of the Seismological Society of America* **57**, 341 (1967).
20. Mello, M., Bhat, H. S., Rosakis, A. J. & Kanamori, H. Identifying the unique ground motion signatures of supershear earthquakes: theory and experiments. *Tectonophysics* **494**, 297–326 (2010).
21. Freund, L. B. The mechanics of dynamic shear crack propagation. *J. Geophys. Res.* **84**, 2199–2209 (1979).
22. Peng, Z. & Gomberg, J. An integrated perspective of the continuum between earthquakes and slow-slip phenomena. *Nature Geosci.* **3**, 599–607 (2010).
23. Obara, K. Nonvolcanic deep tremor associated with subduction in southwest Japan. *Science* **296**, 1679–1681 (2002)
24. Rogers, G. & Dragert, H. Episodic tremor and slip on the Cascadia subduction zone: The chatter of silent slip. *Science* **300**, 1942–1943 (2003).
25. Shelly, D. R., Beroza, G. C. & Ide, S. Non-volcanic tremor and low frequency earthquake swarms. *Nature* **446**, 305–307 (2007).
26. Dragert, H., Wang, K. & James, T. S. A silent slip event on the deeper Cascadia subduction interface. *Science* **292**, 1525–1528 (2001).
27. Ide, S., Beroza, G. C., Shelly, D. R. & Uchide, T. A scaling law for slow earthquakes. *Nature* **447**, 76–79 (2007).
28. Voisin, C., Grasso, J. R., Larose, E. & Renard, F. Evolution of seismic signals and slip patterns along subduction zones: Insights from a friction lab scale experiment. *Geophys. Res. Lett.* **35**, L08302 (2008).
29. Ghaffari, H. O. & Young, R. P. Network configurations of dynamic friction patterns. *EPL* **98** (4), 48003 (2012).
30. Ghaffari, H. O. & Young, R. P. Topological complexity of frictional interfaces: friction networks. *Nonlinear Processes Geophys.* **19**, 215 (2012).
31. Thompson, B. D., Young, R. P. & Lockner, D. A. Observations of premonitory acoustic emission and slip nucleation during a stick slip experiment in smooth faulted Westerly granite. *Geophys. Res. Lett.* **32**, L10304 (2005).
32. Thompson, B. D., Young, R. P. & Lockner, D. A. Premonitory acoustic emissions and stick-slip in natural and smooth-faulted Westerly granite. *J Geophys Res.* **114**, B02205J (2009).
33. Iwayama, K. *et al.* Characterizing global evolutions of complex systems via intermediate network representations. *Scientific Reports* **2**, 423 (2012).
34. McGraw, P. N. & Menzinger, M. Laplacian spectra as a diagnostic tool for network structure and dynamics. *Phys. Rev. E* **77**, 031102 (2008).
35. Newman, M. E. J. *Networks: An Introduction* (Oxford University Press, 2010).
36. Guimerà, R. & Amaral, L. A. N. Functional cartography of complex metabolic networks. *Nature.* **433**, 895–900 (2005).
37. Newman, M. E. J. & Girvan, M. Finding and evaluating community structure in networks. *Phys. Rev. E* **69**, no. 026113 (2004).
38. Fortunato, S. Community detection in graphs. *Phys. Rep.* **486**, 75–174 (2010).
39. Sethna, J. P., Dahmen, K. A. & Myers, C. R. Crackling noise. *Nature.* **410**, 242–250 (2001).
40. Mehta, A. P., Mills, A. C., Dahmen, K. A. & Sethna, J. P. Universal pulse shape scaling function and exponents: Critical test for avalanche models applied to Barkhausen noise. *Physical Review E.* **65** (4), 046139 (2002).
41. Livne, A., Cohen, G. & Fineberg, J. Universality and hysteretic dynamics in rapid fracture. *Physical review letters* **94** (22), 224301 (2005).
42. Nakao, H. & Mikhailov, A. S. Turing patterns in network-organized activator-inhibitor systems. *Nature Phys.* **6**, 544–550 (2010).
43. Zhang, J. & Small, M. Complex network from pseudoperiodic time series: topology versus dynamics. *Phys. Rev. Lett.* **96** (23), 238701 (2006).
44. Yang, Y. & Yang, H. Complex network-based time series analysis. *Physica A: Statistical Mechanics and its Applications* **387** (5), 1381–1386 (2008).
45. Lacasa, L., Luque, B., Ballesteros, F., Luque, J. & Nuño, J. C. From time series to complex networks: the visibility graph. *PNAS.* **105** (13), 4972–4975 (2008).
46. Campanharo, A. S., Sirer, M. I., Malmgren, R. D., Ramos, F. M. & Amaral, L. A. N. Duality between time series and networks. *PloS one* **6** (8), e23378 (2011).
47. Xu, X., Zhang, J. & Small, M. Superfamily phenomena and motifs of networks induced from time series. *PNAS.* **105** (50), 19601–19605 (2008).
48. Marwan, N., Donges, J. F., Zou, Y., Donner, R. V. & Kurths, J. Complex network approach for recurrence analysis of time series. *Physics Letters A.* **373** (46), 4246–4254 (2009).
49. Donner, R. V., Zou, Y., Donges, J. F., Marwan, N. & Kurths, J. Recurrence networks—A novel paradigm for nonlinear time series analysis. *New Journal of Physics* **12** (3), 033025(2010).
50. Bassett, D. S., Meyer-Lindenberg, A., Achard, S., Duke, T. & Bullmore, E. Adaptive reconfiguration of fractal small-world human brain functional networks. *PNAS* **103** (51), 19518–19523 (2006).

Acknowledgements

We would like to acknowledge and thank Dr. B.D. Thompson (Mine Design Engineering, Kingston, Canada), Dr. D. Lockner (USGS, Menlo-Park, USA) and Prof. J. Fineberg (The Racah Institute of Physics, Hebrew University of Jerusalem) for providing the employed data set in this work. The authors would like to express appreciation to Prof. K. Xia and Dr.M.H.B.Nasseri (University of Toronto) for their comments and points. We would also like to thank the Natural Sciences and Engineering Research council of Canada for a discovery grant to R.P.Y. that was used in part to found this research.

Author contributions

H.O.G.H. and R.P.Y. designed the research. H.O.G.H. performed the calculations and wrote the manuscript. R.P.Y. supervised the research and the analysis of the results.

Additional information

Supplementary information accompanies this paper at http://www.nature.com/scientificreports

Competing financial interests: The authors declare no competing financial interests.

How to cite this article: Ghaffari, H.O. & Young, R.P. Acoustic-Friction Networks and the Evolution of Precursor Rupture Fronts in Laboratory Earthquakes. *Sci. Rep.* **3**, 1799; DOI:10.1038/srep01799 (2013).